

# The role of material strength in collisions

## Comparing solid body and hydrodynamic physics for simulating collisions of planetesimals with icy shells

T. I. Maindl<sup>1</sup>, R. Dvorak<sup>1</sup>, R. Speith<sup>2</sup>, and C. Schäfer<sup>3</sup>

<sup>1</sup> Institut für Astronomie, Universität Wien, Türkenschanzstraße 17, A-1180 Wien, Austria  
e-mail: thomas.maindl@univie.ac.at, rudolf.dvorak@univie.ac.at

<sup>2</sup> Physikalisches Institut, Eberhard Karls Universität Tübingen, Auf der Morgenstelle 14, 72076 Tübingen, Germany  
e-mail: speith@pit.physik.uni-tuebingen.de

<sup>3</sup> Institut für Astronomie und Astrophysik, Eberhard Karls Universität Tübingen, Auf der Morgenstelle 10, 72076 Tübingen, Germany  
e-mail: christoph.schaefer@tat.uni-tuebingen.de

Received 1 January 2013 / Accepted 1 January 2013

### ABSTRACT

*Context.* We investigate the effects of including material strength in multi-material planetesimal collisions.

*Aims.* The differences between strengthless material models and including the full elasto-plastic model for solid bodies with brittle failure and fragmentation when treating collisions of asteroid-sized bodies as they occur frequently in early planetary systems are demonstrated.

*Methods.* We study impacts of bodies of Ceres-mass with a solid rock target and an impactor with 30 wt% water content. The initial impact velocities and impact parameters are varied between the escape velocity  $v_{\text{esc}}$  to about  $6 v_{\text{esc}}$  and from head-on collisions to close fly-bys, respectively. We simulate the collisions using our own SPH code using both strengthless material and the full elasto-plastic material model including brittle failure.

*Results.* The qualitative analysis results in significant differences depending on whether material strength is included or not. This may be an effect of the relatively low-energy impacts that cannot destroy the solid material instantly. One of the most prominent differences is the higher degree of fragmentation and shattered debris clouds in the solid case. As opposed to giant impacts we also observe some water ice to get transferred from the impactor to the target.

**Key words.** Methods: numerical - Minor planets, asteroids: general - Planets and satellites: formation

## 1. Introduction

Existing dynamic studies on the evolution of planetesimals and protoplanets targeting the formation of terrestrial planets assume perfectly inelastic merging (cf. Lunine et al. 2011) or simplified fragmentation models (e.g., Alexander & Agnor 1998) whenever a collision occurs. By analyzing the bodies' angular momentum Agnor et al. (1999) showed that the assumption of perfectly inelastic merging cannot be sustained as it would lead to rotationally unstable bodies. The true outcome of a collision depends on parameters like the masses involved, collision speed, and the impact angle and can be categorized in one of the four regimes efficient accretion/perfect merging, partial accretion, hit-and-run, and erosion and disruption (Asphaug 2010). Accretion efficiency of giant impacts was studied e.g., by Agnor & Asphaug (2004) who investigated collision outcomes of two  $0.1 M_{\oplus}$  bodies with different speeds and impact angles using smoothed particle hydrodynamics (SPH) simulations. Marcus et al. (2009) extend disruption criteria for giant impacts up to a body mass of  $10 M_{\oplus}$ . All in all it is found that 40–50% of giant collisions are actually not merging events (Agnor & Asphaug 2004; Genda et al. 2012; Kokubo & Genda 2010).

Marcus et al. (2010) show that water contents cannot increase from giant impacts of bodies with masses  $0.5 \dots 5 M_{\oplus}$ . As

we are interested in possible water delivery by impacts in early planetary systems we have to look at collision events of smaller bodies, typically involving lower energy and the possibility of water (ice) being transferred between the impactors. Like in the case of planet formation, previous studies simulating the dynamics and collision statistics of asteroid families during and after the Late Heavy Bombardment in the early solar system (e.g., Dvorak et al. 2012) assume perfect merging and complete delivery of the asteroids' water content to the impact target. Knowing that this assumption does not hold we need to closely investigate the impact process itself in order to define the conditions under which water is actually transferred rather than being lost during a smaller-scale collision.

For the detailed impact simulations we chose to follow the aforementioned studies on giant collisions and deploy the smooth(ed) particle hydrodynamics (SPH) method, a meshless Lagrangian particle method developed by Lucy (1977) and Gingold & Monaghan (1977) for simulating compressible flows in astrophysical context. For a detailed description of SPH see, e.g., Monaghan (2005); Rosswog (2009); Schäfer et al. (2004). Most giant impact studies treat the colliding bodies as strengthless (e.g., Canup et al. 2013) by applying the hydro parts of the physical equations defining the material behavior during the impacts. The reasoning is based on the assumption that in giant impacts

self-gravity dominates the effects of tensile strength of the material so that hydrodynamics are sufficient to describe the physical effects (e.g., Marcus et al. 2009). Melosh & Ryan (1997) find a size limit of 400 m in radius for basaltic objects beyond which the energy required to disrupt an asteroid is larger than the energy that is needed for shattering it (i.e., overcoming its tensile strength). Other strengthless models of protoplanet collisions assume a parameter measuring the momentum exchange during the collision and that depends on the bodies' material and size (e.g., parameter  $\alpha$  in Genda et al. 2012). The objects we are dealing with however, have masses of the order of magnitude of  $M_{\text{Ceres}}$  and accordingly smaller impact velocities and energies than in the case of giant collisions. Also, we are interested in the details in the collision outcome such as material transfer which is beyond distinguishing between disruption and shattering so that we expect a noticeable contribution of material strength to the simulation outcome.

We use a solid state continuum mechanics model as introduced in SPH by Libersky & Petschek (1991), extended by a model for simulating brittle failure (Benz & Asphaug 1994, 1995), and successfully applied to simulating planetary and asteroid dynamics (cf. Benavidez et al. 2012; Michel et al. 2004; Jutzi & Asphaug 2011, and references therein). SPH has also been used successfully for simulating impacts involving agglomerates such as homogeneous protoplanetesimals and comets (Geretshausen et al. 2011; Jutzi et al. 2008, 2009; Schäfer et al. 2007). In this study we focus on identifying the difference the full elasto-plastic model including a damage model for brittle failure and fragmentation makes compared to hydrodynamic treatment of the material when studying collisions of solid, Ceres-sized bodies with water (ice) content.

This paper introduces the two physical models for elasto-plastic continuum mechanics with brittle failure and the hydrodynamic equations in Sect. 2. In Sect. 3 we briefly discuss our SPH code and describe the simulation scenarios. In Sect. 4 we compare the simulation results for the two physical models phenomenologically and conclude in Sect. 5, also presenting identified subjects of future more detailed quantitative studies.

## 2. The physical model

### 2.1. Elasto-plastic materials and brittle failure

For describing the dynamics of solid bodies we use the equations governing the conservation of mass, momentum, and energy formulated according to the theory of continuum mechanics (see for example, Schäfer et al. 2007). For legibility we use the Einstein summation convention and omit particle indices so that the continuity equation in Lagrangian form is

$$\frac{d\rho}{dt} + \rho \frac{\partial v^\alpha}{\partial x^\alpha} = 0 \quad (1)$$

with the density  $\rho$  and velocity and positional coordinates  $v^\alpha$  and  $x^\alpha$ , respectively. In the case of a solid body the stress tensor  $\sigma^{\alpha\beta}$  takes the role of the pressure  $p$  and momentum conservation reads

$$\frac{dv^\alpha}{dt} = \frac{1}{\rho} \frac{\partial \sigma^{\alpha\beta}}{\partial x^\beta}, \quad \sigma^{\alpha\beta} = -p \delta^{\alpha\beta} + S^{\alpha\beta} \quad (2)$$

with the deviatoric stress tensor  $S^{\alpha\beta}$  and the Kronecker delta  $\delta^{\alpha\beta}$ . According to Hooke's law the time evolution of the deviatoric stress tensor is given by the constitutive equations

$$\frac{dS^{\alpha\beta}}{dt} = 2\mu \left( \dot{\epsilon}^{\alpha\beta} - \frac{1}{3} \delta^{\alpha\beta} \dot{\epsilon}^{\gamma\gamma} \right) + S^{\alpha\gamma} R^{\gamma\beta} - R^{\alpha\gamma} S^{\gamma\beta} \quad (3)$$

where  $\dot{\epsilon}^{\alpha\beta}$  is the strain rate tensor

$$\dot{\epsilon}^{\alpha\beta} = \frac{1}{2} \left( \frac{\partial v^\alpha}{\partial x^\beta} + \frac{\partial v^\beta}{\partial x^\alpha} \right) \quad (4)$$

and the rotation rate tensor  $R^{\alpha\beta}$  is necessary to make the constitutive equations independent from the material frame of reference:

$$R^{\alpha\beta} = \frac{1}{2} \left( \frac{\partial v^\alpha}{\partial x^\beta} - \frac{\partial v^\beta}{\partial x^\alpha} \right). \quad (5)$$

Conservation of specific inner energy  $u$  of particles constituting a solid body reads

$$\frac{du}{dt} = -\frac{p}{\rho} \frac{\partial v^\alpha}{\partial x^\alpha} + \frac{1}{\rho} S^{\alpha\beta} \dot{\epsilon}^{\alpha\beta}. \quad (6)$$

For closing this set of partial differential equations an equation of state (EOS) connecting pressure, density, and specific energy of the form  $p = p(\rho, u)$  is required. In this work we use the non-linear Tillotson EOS (Tillotson 1962) as given in Melosh (1989). It depends on 10 material constants  $\rho_0$ ,  $A$ ,  $B$ ,  $a$ ,  $b$ ,  $\alpha$ ,  $\beta$ ,  $E_0$ ,  $E_{iv}$ , and  $E_{cv}$  and distinguishes three domains: in compressed regions ( $\rho > \rho_0$ ) and  $u$  lower than the incipient vaporization specific energy  $E_{iv}$  the pressure is given by

$$p(\rho, u) = \left[ a + \frac{b}{1 + u/(E_0 \eta^2)} \right] \rho u + A \mu_T + B \mu_T^2 \quad (7)$$

with  $\eta = \rho/\rho_0$  and  $\mu_T = \eta - 1$ . In the expanded state where  $u$  is greater than the specific energy of complete vaporization  $E_{cv}$  it reads

$$p(\rho, u) = a \rho u + \left[ \frac{b \rho u}{1 + u/(E_0 \eta^2)} + \frac{A \mu_T}{e^{\beta(\rho_0/\rho-1)}} \right] e^{-\alpha(\rho_0/\rho-1)^2}. \quad (8)$$

In the partial vaporization domain i.e.,  $E_{iv} \leq u \leq E_{cv}$ , the pressure  $p$  is linearly interpolated between the values obtained via (7) and (8), respectively.

Equations (1)–(8) describe the dynamics of a body in the elastic regime. For modeling plastic behavior we apply the von Mises yielding criterion  $S^{\alpha\beta} S^{\alpha\beta} > \frac{2}{3} Y^2$  (see Benz & Asphaug 1994) which uses the material yield stress  $Y$  to limit the deviatoric stress tensor. Hence, we use a transformed deviatoric stress tensor

$$S^{\alpha\beta} \rightarrow \frac{2 Y^2}{3 S^{\gamma\delta} S^{\gamma\delta}} S^{\alpha\beta} \quad (9)$$

if the von Mises criterion is fulfilled.

We model fracture of the material by adopting the Grady-Kipp fragmentation model (Grady & Kipp 1980) following the implementation by Benz & Asphaug (1994). It is based on flaws which are assigned to each SPH particle and which can be activated by a certain strain level  $\epsilon$ . Once active, they develop into cracks and contribute to the damage value  $d \in [0, 1]$  of a SPH particle which is defined as the ratio of cracks to flaws. The deviatoric stress is reduced proportional to  $1 - d$  and hence vanishes for totally damaged material ( $d = 1$ ). The initial distribution of the number of flaws  $n$  with activation threshold  $\epsilon$  follows a Weibull distribution

$$n(\epsilon) = k \epsilon^m \quad (10)$$

with material parameters  $k$  and  $m$  (Weibull 1939).

We will use the term *solid model* when we refer to the model defined by the equations of this Sect. 2.1.

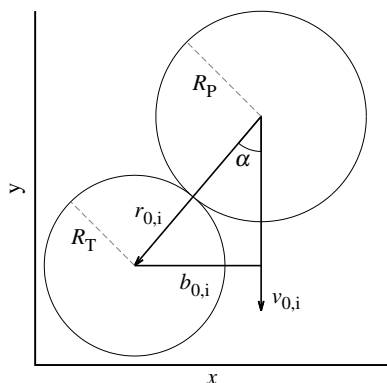


**Fig. 1.** Collision geometry schematic in the target’s rest frame. The centers of the two bodies are in the  $xy$ -plane; the impact velocity vector  $\mathbf{v}_{0,i}$  is parallel to the  $y$ -axis and the impact speed is  $v_{0,i} = |\mathbf{v}_{0,i}|$ . The impact angle  $\alpha$  is defined as the angle between  $\mathbf{v}_{0,i}$  and the vector  $\mathbf{r}_{0,i}$  connecting the two centers upon impact ( $\cos \alpha = \left| \frac{\mathbf{r}_{0,i} \cdot \mathbf{v}_{0,i}}{r_{0,i} v_{0,i}} \right|$ ,  $r_{0,i} = R_T + R_P = |\mathbf{r}_{0,i}|$ ) and related to the impact parameter upon collision by  $b_{0,i} = r_{0,i} \sin \alpha$ .

## 2.2. The hydro model

In order to model strengthless bodies we use the equations of Sect. 2.1 neglecting deviatoric stress, which eliminates Hooke’s law, plastic behavior and the damage model. The equations reduce to

$$\frac{d\rho}{dt} + \rho \frac{\partial v^\alpha}{\partial x^\alpha} = 0, \quad \frac{dv^\alpha}{dt} = -\frac{1}{\rho} \frac{\partial p}{\partial x^\alpha}, \quad \frac{du}{dt} = -\frac{p}{\rho} \frac{\partial v^\alpha}{\partial x^\alpha} \quad (11)$$

along with the EOS as defined in Eqs. (7) and (8).

We will use the term *hydro model* when we refer to the model defined by the equations of this Sect. 2.2.

Additionally, viscous effects are considered according to the usual SPH artificial viscosity terms in both the solid and hydro models.

## 3. Numerical simulations

All simulations are performed with our own 3D parallel SPH code as introduced in Maindl et al. (2013) with further improvements of performance. The simulations include self-gravity which is needed as we are interested in the global outcome of collisions of bodies of comparable size as opposed to damage done to a target by a high-velocity small body. We ensure first order consistency and angular momentum conservation by correcting the rotation rate and strain rate tensors as described in Schäfer et al. (2007).

The collisions involve spherical targets and projectiles composed of basalt and water ice. Because of the bodies’ spherical symmetry the collisions can be described by the impact angle  $\alpha$  or equivalently, the impact parameter  $b_{0,i}$  and the impact velocity  $v_{0,i}$  as illustrated in Fig. 1 along with the respective target and projectile radii  $R_T$  and  $R_P$ . Initially neither of the bodies is rotating.

For the Tillotson EOS parameters as well as the shear and bulk moduli we adopt the values given in Benz & Asphaug (1999) as summarized in Table 1. Following the reasoning in Maindl et al. (2013) the Weibull distribution parameters of basalt were set to measured values of Nakamura et al. (2007) and for ice we use those mentioned in Lange et al. (1984), see Table 2.

The masses of the projectile and target  $M_P$  and  $M_T$ , respectively are assumed to be equal and are fixed to Ceres’ mass. We

**Table 2.** Weibull distribution parameters.

Material	$m$	$k$ [ $\text{m}^{-3}$ ]	Reference
Basalt	16	$10^{61}$	(1)
Ice	9.1	$10^{46}$	(2)

**References.** (1) Nakamura et al. (2007); (2) Lange et al. (1984).

use  $M_{\text{Ceres}} = 4.74 \cdot 10^{-10} M_\odot = 9.43 \cdot 10^{20}$  kg which is consistent with Baer & Chesley (2008). While the target is a solid basalt body the projectile has a basalt core and a shell of water ice that amounts for  $C_P = 30\%$  of its mass. This will allow us to study possible water transfer by the collision. Accordingly, the projectile radius given by

$$R_P = \sqrt[3]{\left[ C_P + (1 - C_P) \frac{\rho_i}{\rho_b} \right] M_P \frac{3}{4\pi} \frac{1}{\rho_i}} \quad (12)$$

with the respective densities of basalt and ice  $\rho_b$  and  $\rho_i$  is somewhat larger than the target’s radius  $R_T$  (509 km as opposed to 437 km).

In order to cover a large portion of possible collision outcomes for a  $M_P : M_T = 1 : 1$  mass ratio of projectile and target (see Fig. 10 in Leinhardt & Stewart 2012) we arrange our simulations along a grid in initial velocities  $v_0$  w. r. t. the target’s rest frame and initial impact parameters  $b_0$ . The simulations start with the projectile at a central distance of  $r_0 = 5(R_T + R_P) = 4730$  km from the target. Hereby we warrant that projectile and target SPH particles do not interact with the respective other bodies’ SPH particles in the beginning. Additionally, the two bodies will approach their respective internal equilibrium before the impact occurs. According to typical collision speeds of  $M_{\text{Ceres}}$ -bodies as determined in Maindl & Dvorak (2013) by means of  $n$ -body simulations, initial velocities are chosen in seven steps covering a range from the target’s escape velocity at the initial location of the projectile (231 m/s) up to 3 km/s. Six steps were chosen for  $b_0$  covering central impacts ( $b_0 = 0$ ) up to fly-bys ( $b_0 = 2[R_P + R_T] = 1,892$  km). Table 3 gives the specific initial values that define the parameter grid. The largest  $b_0$  value was chosen to allow studying close encounters and estimate the influence of mutual gravity onto the actual velocities and impact angles.

Each of the scenarios defined by  $v_0$  and  $b_0$  was simulated over a period of  $1.2 \cdot 10^5$  s in both the solid and hydro models using an adaptive time step integration scheme in a barycentric frame with output snapshots every 30 seconds resulting in a total of 84 scenarios. For the qualitative investigations we resolve the system in 20,000 SPH particles following Agnor & Asphaug (2004) and the reasoning in Nouda et al. (2009). Also, Genda et al. (2012) studied how critical impact velocities depend on the particle numbers and established slight differences for low-resolution scenarios (3,000 particles) and only negligible variations for particle numbers between 20,000 and 100,000. Computation time of our parallel code on contemporary 8-core CPUs ranges from just under a day to three weeks per scenario depending on the modeled physics, number of interacting SPH particles, relative velocities, etc. Typically, the solid model is computationally more expensive than the hydro model by about one order of magnitude due to the considerably more complex physics.

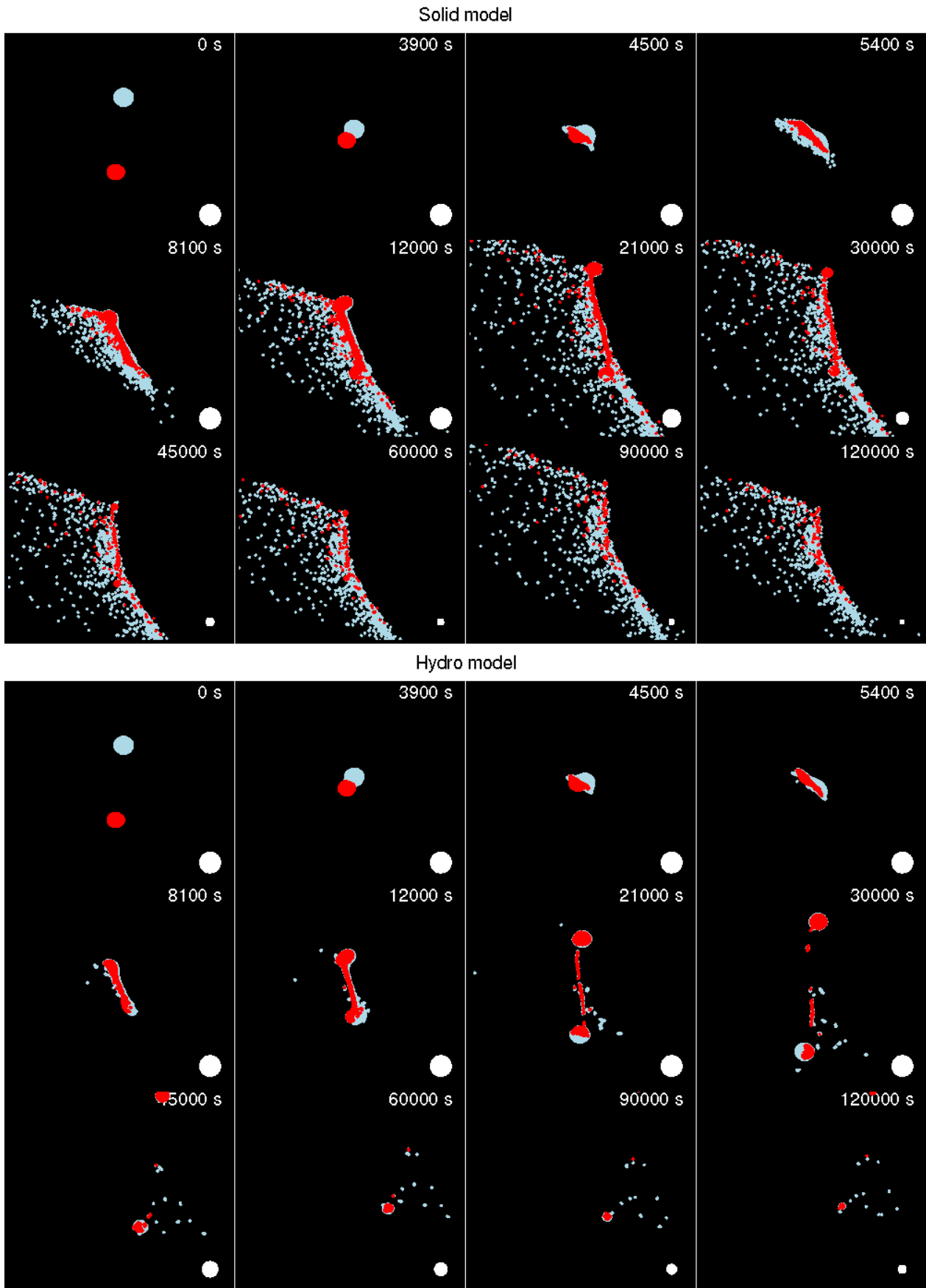


**Fig. 2.** Snapshots of the  $b_0 = 437$  km,  $v_0 = 1000$  m/s scenario (top: solid, bottom: hydro model). The white disc in the bottom right corner indicates the size of the projectile as the scale changes, the time stamp gives the number of seconds passed since simulation start. See text for explanation.

**Table 1.** Tillotson EOS parameters, shear modulus  $\mu$ , and yield stress  $Y$  in SI units (Benz & Asphaug 1999). Note that  $A$  and  $B$  are set equal to the bulk modulus.

Material	$\rho_0$ [kg m <sup>-3</sup> ]	$A$ [GPa]	$B$ [GPa]	$E_0$ [MJ kg <sup>-1</sup> ]	$E_{iv}$ [MJ kg <sup>-1</sup> ]	$E_{cv}$ [MJ kg <sup>-1</sup> ]	$a$	$b$	$\alpha$	$\beta$	$\mu$ [GPa]	$Y$ [GPa]
Basalt	2700	26.7	26.7	487	4.72	18.2	0.5	1.50	5.0	5.0	22.7	3.5
Ice	917	9.47	9.47	10	0.773	3.04	0.3	0.1	10.0	5.0	2.8	1

**Table 3.** Initial conditions of the impact simulations. At the beginning the colliding bodies are  $r_0 = 5(R_T + R_P) = 4730$  km apart: (a) Initial velocities  $v_0$  with normalization by the two-body escape velocity at the initial distance  $r_0$ , (b) Initial impact parameters  $b_0$  and hypothetical impact angle  $\alpha_0$  (neglecting gravitational interaction, for information only).

(a)		(b)		
$v_0$ [m s <sup>-1</sup> ]	$\frac{v_0}{v_{esc}(r_0)}$	$b_0$ [km]	Comment	$\alpha_0$ [°]
231	1	0	head-on	0
516 <sup>a</sup>	2.23	219	$\frac{1}{2}R_T$	13
537 <sup>b</sup>	2.32	437	$R_T$	28
1000	4.33	819	-	60
1500	6.49	946	$R_P + R_T$	90
2000	8.66	1892	$2(R_P + R_T)$	fly-by
3000	12.99			

**Notes.** <sup>(a)</sup> Two-body escape velocity upon contact <sup>(b)</sup> Target's surface escape velocity

## 4. Simulation results

Throughout the scenarios we observe significant qualitative differences between the solid and hydro models. Where in the hydro case fragments of the shape of “bubbles” are ejected upon impact the solid model resembles the formation of dust-like debris clouds and solid fragments that themselves accrete debris and grow. Figures 2 and 3 illustrate the model differences for two selected scenarios. In both the bodies survive the collision and escape due to high collision velocities. The solid models result in shattering of the body mantles and primarily water being ejected in Fig. 2 while due to a high rotation rate in the solid model part of Fig. 3 also a basalt debris cloud is forming after the impact. See Sect. 4.2 for a systematic description of the scenario results.

In analyzing the results the resolution of the method has to be kept in mind. Given the total number of SPH particles resolving the initially homogeneous basalt and water ice along with our choice for the kernel's smoothing length<sup>1</sup> the spatial resolution is about 70 km.

Immediately after starting the simulations an increase in overall damage is noticeable. This is due to internal forces that establish a density gradient primarily driven by self-gravity; in the fly-by scenarios additional tidal forces act upon the bodies during the close encounter contributing to increasing damage values. At the instance of the impact and shortly after, the overall damage quickly rises and gets saturated at a level very close to 1 as illustrated in Fig. 4a–e and by the  $v_0 = 231$  m/s line in Fig. 4f (colliding scenarios). In case of a near miss ( $v_0 \geq 516$  m/s in

<sup>1</sup> In this study the smoothing length is constant in time and across materials (our choice for the total number of SPH particles results in a separation of approx. 35 km in the initial particle distribution; the smoothing length factor is 2.01).

**Table 5.** Actual impact velocities  $v_{0,i}$  for the head-on collision scenarios ( $b_0 = 0$ , initial velocity  $v_0$ , see text).

$v_0$ [m s <sup>-1</sup> ]	hydro		solid	
	$v_{0,i}$ [m s <sup>-1</sup> ]	$\frac{v_{0,i}}{v_{esc}}$	$v_{0,i}$ [m s <sup>-1</sup> ]	$\frac{v_{0,i}}{v_{esc}}$
231	492	0.95	496	0.96
516	679	1.32	685	1.33
537	694	1.34	700	1.36
1000	1096	2.12	1096	2.12
1500	1566	3.04	1566	3.04
2000	2045	3.96	2048	3.97
3000	3032	5.88	3032	5.88

Fig. 4f) the damage value increases on a longer timescale due to tidal forces between the bodies.

### 4.1. Actual impact parameters and velocities

As the simulation starts with the two bodies set apart by  $5(R_T + R_P) = 4730$  km the actual impact angles  $\alpha$  (or equivalently, impact parameters  $b_{0,i}$ , cf. Fig. 1) and velocities  $v_{0,i}$  will depend on mutual gravitational interaction and tidal forces while the bodies approach each other. Table 4 gives the actual values for  $\alpha$  and  $v_{0,i}$  that were determined at the time of first interaction between the projectile and target SPH particles in the different scenarios corresponding to inclined impacts. Note that as expected for the largest initial offset  $b_0 = 2(R_P + R_T)$  a collision only occurs for small initial velocities close to the escape velocity; otherwise we observe a fly-by. Table 5 gives the actual collision velocities for the head-on collisions. Note that due to lacking material strength there is more energy dissipated into internal (deformation-) energy in the hydro model than in the solid model. Hence, the actual collision velocities are systematically smaller in the hydro case. This effect is most noticeable in the “slow” scenarios.

Figure 5 shows how the scenarios cover the initial conditions for expected major collision outcomes in the map of collision regimes (cf. Leinhardt & Stewart 2012). For this, the impact velocity was normalized using the two-body escape velocity at the instance of first contact:  $v_{esc}^2 = 2G(M_P + M_T)/(R_P + R_T)$ ,  $v_{esc} = 516$  m/s. Tables 4 and 5 also include the individual velocities in units of  $v_{esc}$ .

### 4.2. Scenario results

In the head-on collisions the difference between the solid and hydro models is most prominent for slow encounters. In the hydro case the two planetesimals merge perfectly for impact velocities  $v_{0,i} \leq 2.12 v_{esc}$  whereas we observe partial erosion in the solid case. In the latter case primarily the water ice layer on the projectile is destroyed and with larger encounter velocities more and more material – primarily ice but also some rocky material – es-

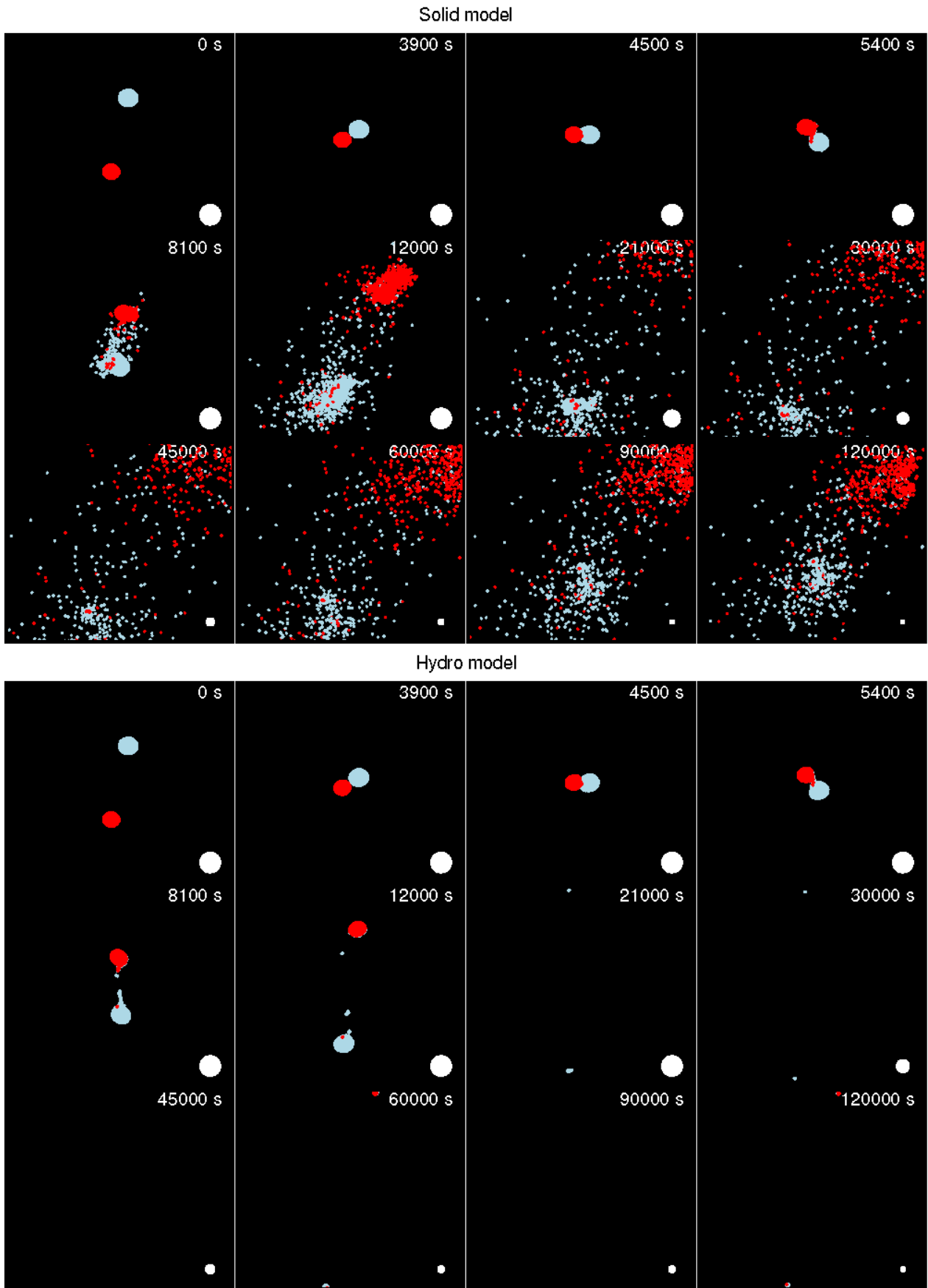


**Fig. 3.** Snapshots of  $b_0 = 946$  km,  $v_0 = 1000$  m/s scenario (top: solid, bottom: hydro model). The white disc in the bottom right corner indicates the size of the projectile as the scale changes, the time stamp gives the number of seconds passed since simulation start. See text for explanation.

**Table 4.** Actual values for the impact angles  $\alpha$  and collision velocities  $v_{0,i}$  for the inclined-collision scenarios defined by initial velocities  $v_0$  and initial impact parameters  $b_0$  (see text).

$v_0$ [ $m s^{-1}$ ]	Model	$b_0$ [km]			437			819			946			1892		
		$\alpha$ [ $^\circ$ ]	$v_{0,i}$ [ $m s^{-1}$ ]	$\frac{v_{0,i}}{v_{esc}}$	$\alpha$ [ $^\circ$ ]	$v_{0,i}$ [ $m s^{-1}$ ]	$\frac{v_{0,i}}{v_{esc}}$	$\alpha$ [ $^\circ$ ]	$v_{0,i}$ [ $m s^{-1}$ ]	$\frac{v_{0,i}}{v_{esc}}$	$\alpha$ [ $^\circ$ ]	$v_{0,i}$ [ $m s^{-1}$ ]	$\frac{v_{0,i}}{v_{esc}}$	$\alpha$ [ $^\circ$ ]	$v_{0,i}$ [ $m s^{-1}$ ]	$\frac{v_{0,i}}{v_{esc}}$
231	hydro	6	490	0.95	11	486	0.94	21	486	0.94	25	486	0.94	58	488	0.95
	solid	14	435	0.84	23	472	0.91	25	513	0.99	31	505	0.98	62	509	0.99
516	hydro	9	677	1.31	19	676	1.31	37	675	1.31	44	675	1.31	-	-	-
	solid	11	686	1.33	21	680	1.32	40	682	1.32	48	681	1.32	-	-	-
537	hydro	9	691	1.34	19	690	1.34	38	690	1.34	45	690	1.34	-	-	-
	solid	11	704	1.37	20	699	1.36	40	697	1.35	48	694	1.34	-	-	-
1000	hydro	12	1094	2.12	24	1095	2.12	48	1094	2.12	59	1092	2.12	-	-	-
	solid	12	1095	2.12	25	1096	2.12	50	1098	2.13	62	1095	2.12	-	-	-
1500	hydro	12	1566	3.04	25	1565	3.03	51	1564	3.03	65	1564	3.03	-	-	-
	solid	12	1566	3.03	25	1566	3.03	53	1567	3.04	67	1567	3.04	-	-	-
2000	hydro	13	2049	3.97	27	2050	3.97	55	2050	3.97	69	2049	3.97	-	-	-
	solid	13	2050	3.97	27	2050	3.97	55	2049	3.97	72	2051	3.98	-	-	-
3000	hydro	13	3034	5.88	28	3031	5.87	58	3034	5.88	72	3033	5.88	-	-	-
	solid	13	3033	5.88	28	3031	5.87	58	3033	5.88	72	3033	5.88	-	-	-

capas into the surrounding environment. Nevertheless the two bodies merge.

For larger encounter velocities the hydro model leads to partial destruction of the bodies and to a good part of the water escaping. In the solid model all the water is lost and mutual destruction of the bodies increases with higher velocities up to total disruption at  $v_{0,i} = 5.88 v_{esc}$ .

As expected for off-center impacts, the newly formed bodies rotate. Otherwise, in the overall picture the cases of slightly off-center impacts ( $\alpha_0 \lesssim 15^\circ$ ) and head-on collisions are similar. Initial velocities up to about 1 km/s lead to virtually lossless merging in the hydro case in contrast to the results from the solid case suggesting a higher velocity-limit for merging of strengthless bodies than suggested by the dashed line in Fig. 5. For higher encounter velocities the codes show similar behavior, mutual destruction can be observed for  $v_{0,i} \gtrsim 3.03 v_{esc}$  which is consistent with the onset of the erosion/disruption regime in Fig. 5.

Further increasing the impact parameter ( $b_0 = R_T = 437$  km) yields impact angles of  $\alpha = 11 \dots 28^\circ$ . In both the solid and hydro models a material bridge between the planetesimals is formed for collision velocities between 2.12 and 3.03  $v_{esc}$ . Because of gravitational attraction this bridge eventually breaks and the respective bodies re-accrete the material. The water ice is not lost in the hydro case whereas in the solid case most of it escapes into the environment. In neither case the bodies merge and both planetesimals survive as separate bodies (partial accretion in Fig. 5).

For lower encounter velocities close to  $v_{esc}$  we observe complete merging in both the hydro and solid cases. Again, from the beginning of the collision (just after the first contact) the water ice deficiency is large in the solid model whereas little water is lost in the hydro case. After merging we observe a quickly rotating spheroid which develops into a spherical body due to self-gravitation / tidal forces, seemingly without water loss in the hydro case. At a higher initial offset of  $b_0 = 819$  km and initial velocity  $v_0 = 231$  m/s we observe a notable difference between the physical models: while perfect merging into a (rotating) body

happens in the hydro case, the solid case yields a high rotation rate of the newly formed spheroidal body that causes a loss of a large fraction of the water ice and some rocky material which is captured again later. One possible explanation for this behavior is in the slightly different actual collision speeds very close to the escape velocity (0.94 and 0.99  $v_{esc}$ , respectively, see Tab. 4) which originate from the different strength models.

While we observe mutual destruction of the bodies for larger impact velocities  $\geq 3.97 v_{esc}$  and  $\alpha = 27 \dots 28^\circ$ , this does not happen any more when the actual impact angle is beyond the onset for hit-and-run collisions around a  $30^\circ$  impact angle.

For collision velocities  $\lesssim v_{esc}$  we expect merging, which we also observe in the simulations. Higher velocities between 1.3 and 1.4  $v_{esc}$  and impact angles between  $37$  and  $40^\circ$  lead to notable results: In the  $b_0 = 819$  km,  $v_0 = 516$  m/s case illustrated in Fig. 6 both models result in a material bridge forming. The resulting dumbbell-like body rotates quickly and again loses primarily water in the solid case while approaching a spherical shape. In the hydro case the material bridge breaks at about 350 minutes into the simulation, but soon after the bodies merge as sufficient linear kinetic energy has been converted into rotational and internal deformation energy, which is consistent with prior SPH-based simulations of strengthless larger bodies (planetary embryos) by Agnor & Asphaug (2004). During this process fast rotation occurs which also leads to loss of water and some rocky material in the hydro model. This suggests a somewhat higher velocity limit for merging than predicted in Fig. 5.

Slightly increasing the initial velocity for the same initial impact parameter ( $v_0 = 537$  m/s) results in a similar configuration in the hydro case (at  $\alpha = 38^\circ$ ,  $v_{0,i} = 1.34 v_{esc}$ ) in which more rocky material is lost due to high angular momentum of the newly formed merged body. However, the resulting configuration is completely different in the solid model: the bridge that forms right after the collision breaks apart and the two bodies escape while losing a large fraction of the water marking the onset of hit-and-run in the solid model at  $\alpha = 40^\circ$  and  $v_{0,i}$  between 1.32 and 1.35  $v_{esc}$ . This is in agreement with findings on giant collisions obtained via strengthless-model SPH calculations, see

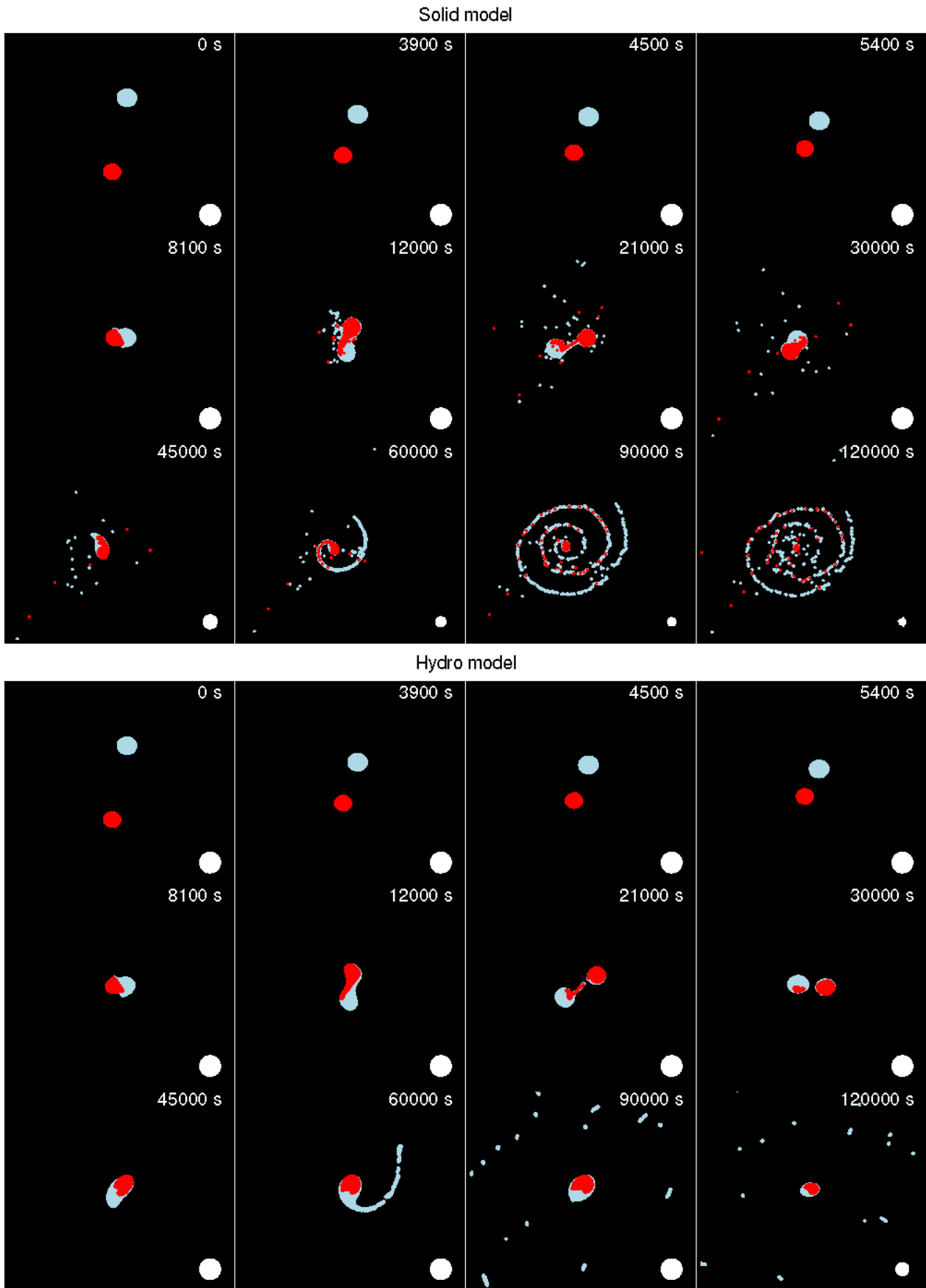


**Fig. 6.** Snapshots of  $b_0 = 819$  km,  $v_0 = 516$  m/s scenario (top: solid, bottom: hydro model). The white disc in the bottom right corner indicates the size of the projectile as the scale changes, the time stamp gives the number of seconds passed since simulation start. See text for explanation.



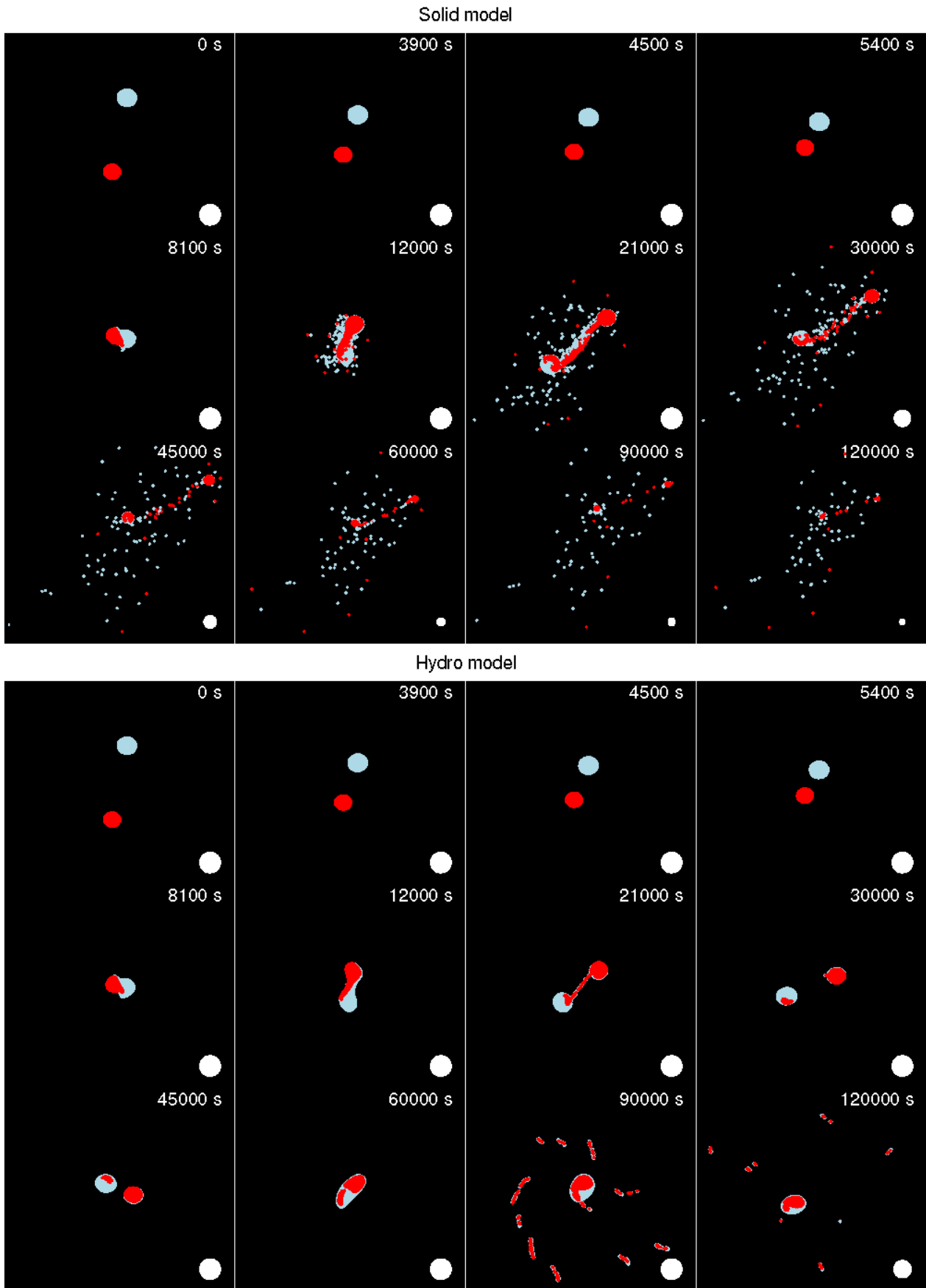


**Fig. 7.** Snapshots of  $b_0 = 819$  km,  $v_0 = 537$  m/s scenario (top: solid, bottom: hydro model). The white disc in the bottom right corner indicates the size of the projectile as the scale changes, the time stamp gives the number of seconds passed since simulation start. See text for explanation.

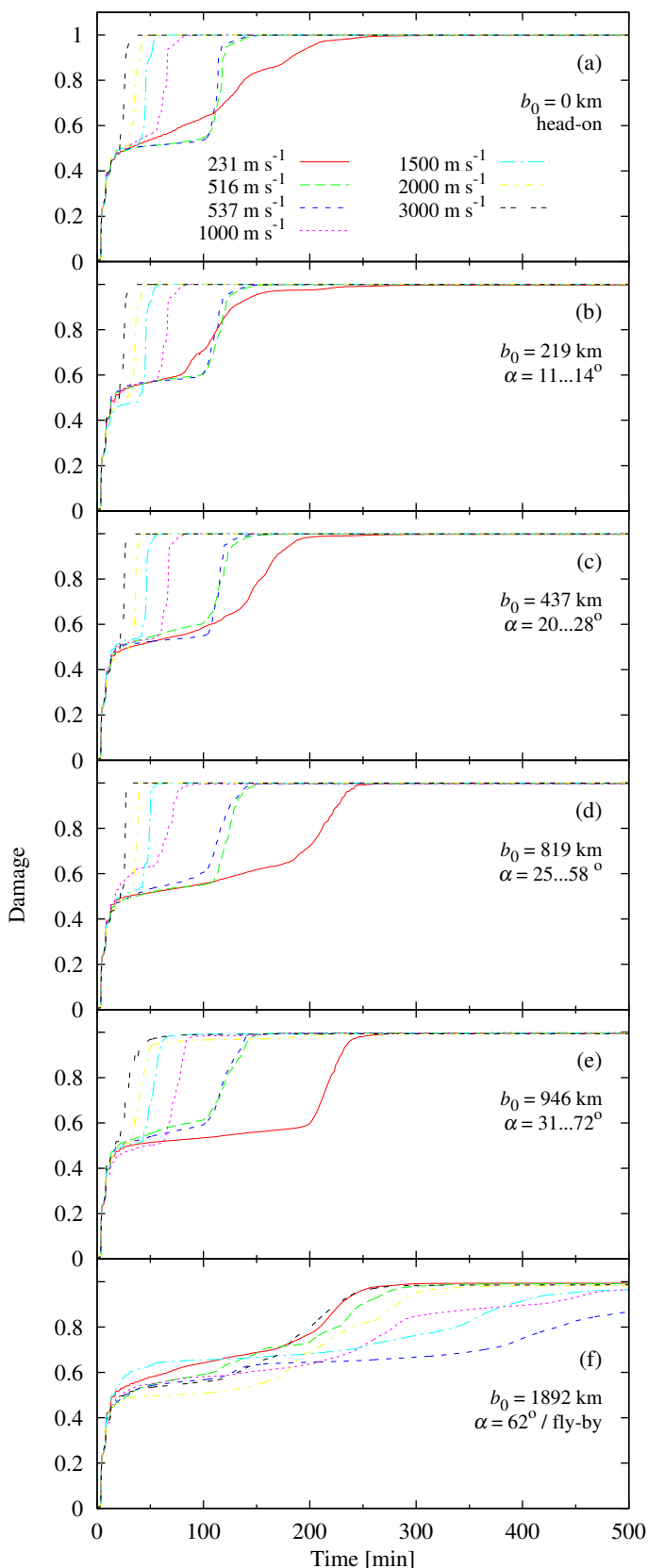


**Fig. 4.** Average damage (cf. Sect. 2.1) per SPH particle 500 minutes into the simulation in the solid scenarios. The different curves correspond to the initial velocities  $v_0$  as indicated in the top frame. After settling at around 0.5 due to tidal forces the collision increases the damage up to almost one in the colliding scenarios ( $b_0 \leq 946$  km and  $v_0 = 231$  m s<sup>-1</sup> in the  $b_0 = 1892$  km case). Note the gradual damage increase due to tidal forces in the fly-by scenarios.

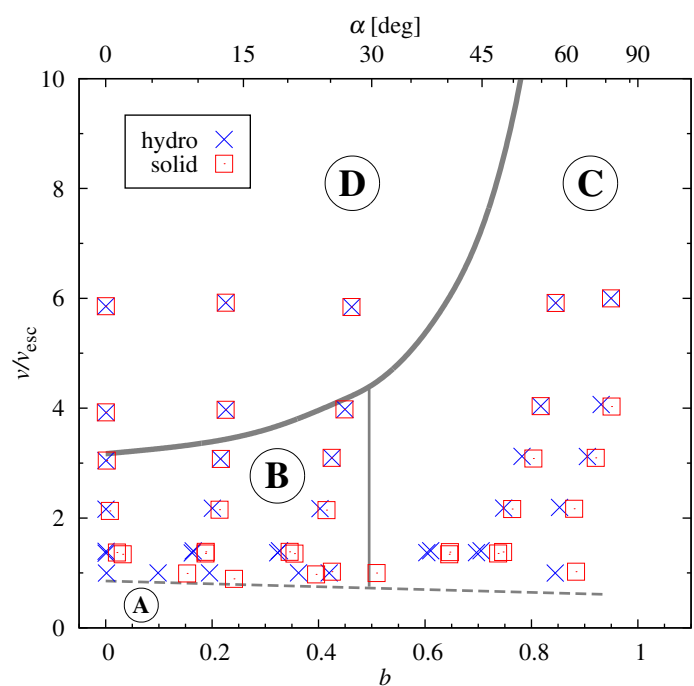


**Fig. 5.** Our simulation scenarios in the map of collision regimes for  $M_p : M_T = 1 : 1$  (cf. Leinhardt & Stewart 2012). Below the dashed line we expect perfect merging (area A), between the dashed and solid curves partial accretion (area B) to the left of the vertical line and hit-and-run collisions to its right (area C). Above the solid curve erosion/disruption is expected (area D). Note that  $\alpha$  is the actual impact angle,  $v_{\text{esc}}$  the two-body escape velocity upon contact and the dimensionless impact parameter  $b = \sin \alpha$  is defined such that  $b = 0$  for a 90° grazing impact.

Fig. 17 of Asphaug (2009) that shows the transition between merging and hit-and-run at  $v_{0,i} \approx 1.41 v_{\text{esc}}$  for  $\alpha = 30^\circ$  and  $v_{0,i} \approx 1.12 v_{\text{esc}}$  for  $\alpha = 45^\circ$ . For higher velocities  $v_{0,i} \geq 2.12 v_{\text{esc}}$  we consistently observe hit-and-run encounters: both models result in the material bridge breaking up and the two bodies escaping each other after losing a large portion of the water.

A further increase in the initial impact parameter  $b_0$  results in the planetesimals merging only for collision velocities smaller than the escape velocity. In case of impact velocities in the  $1.31 \dots 1.34 v_{\text{esc}}$  range the bodies stay together shortly, a material bridge forms, breaks again, and finally the planetesimals escape, strongly deflecting each other’s orbits. Again, debris is sprayed into space in the solid model.

For larger velocities up to  $v_{0,i} \approx 3.04 v_{\text{esc}}$  the bodies just briefly touch each other and escape in the hydro model. In the solid model they also escape; however, the “grazing collision” results in extensive debris clouds consisting of water ice and rocky material covering the planetesimals after the impact. These two clouds move in opposite directions and we predict that eventually there will be two surviving planetesimals, a water-abundant one and a rocky one. It looks like no water is transferred to the target.

In case of even larger encounter velocities  $v_{0,i} \geq 3.97 v_{\text{esc}}$  the hydro and solid models produce very similar outputs: due to the high velocities the impacts are truly grazing and the bodies lose very little ( $v_{0,i} = 3.97 v_{\text{esc}}$  and  $3.98 v_{\text{esc}}$ , resp.) to hardly any ( $v_{0,i} = 5.88 v_{\text{esc}}$ ) material and escape.

Once the initial separation is large enough ( $b_0 = 1892$  km) the planetesimals feel tidal forces but retain enough momentum to escape on hyperbolic orbits around their barycenter if their initial relative velocity is greater than their escape velocity.

In the “slowest”  $v_0 = v_{\text{esc}} = 231$  m/s scenario however, the bodies collide due to mutual gravitational attraction. Due to energy dissipation into internal (deformation-) energy the collision speed is slightly lower than  $v_{\text{esc}}$ . The solid model predicts a material bridge that breaks after one “dumbbell-revolution” to lead to a second collision finally forming a rotating spheroid that loses icy and rocky material while it approaches a spherical shape. This breakup and re-unifying is not predicted by the hydro model where the planetesimals merge to form a spheroid as well that loses light material (water ice) only while it rotates and approaches spherical symmetry.

## 5. Conclusions and future research

We established qualitative differences between collision outcomes obtained by the solid and the hydro models. In general, the solid models predict significantly higher numbers of fragments and dust cloud-like ejecta dispersed over a much greater volume than the collision debris in the hydro case. Also, material – especially water (ice) – loss seems to be bigger in the solid model.

Additionally, our simulations demonstrate that collisions characterized by parameters as they are found by dynamical n-body simulations of early planetary systems can transfer water (ice) from a Ceres-sized projectile to an equally massive target.

As the outcome of the collisions show similarities with existing giant impact results obtained via strengthless solid body models (cf. Sect. 4.2) we feel to have demonstrated that there is need for more detailed quantitative studies to (a) verify our observations regarding the amount of material in general and water (ice) in particular transferred and lost during planetesimal collisions and (b) put them in a quantitative context. For this fragments need to be investigated with respect to their masses and energies determining whether they are bounded to the system of colliding bodies or whether they escape either indefinitely or beyond the system’s Hill radius. As we observe significantly more fragments – also larger ones – in the solid model analyzing the fragment distribution will most likely contribute to investigating the origin of asteroid families from dynamical (cf. Galiazzo et al. 2011) and size statistics (cf. Knežević & Milani 2003) perspectives.

An important question these quantitative studies will answer is whether the difference between the hydro and solid models is large enough to justify the use of solid models when simulating planetesimal collisions in dynamic studies. The latter are significantly more expensive from a computational point of view which will make this a practical issue if we consider working on a “collision outcome catalog” which can subsequently be incorporated in n-body dynamical studies of early planetary systems and will augment using fitted formulas for giant collision outcomes (cf. Genda et al. 2012). The large parameter space that such a catalog will have to cover requires thousands of collision simulations which we plan to tackle deploying a high-performance GPU code. First experiments with our prototype show a speedup by a factor of about 50 compared to the parallel CPU implementation (Riecker 2014).

As we have seen, off-center impacts result in rotating survivors. While there is some indication that more initial linear kinetic energy is converted into internal and/or rotational energy in the hydro model than it is the case in the solid model, more detailed quantitative studies are necessary. Part of these investigations will be studying collision outcomes of initially rotating bodies.

*Acknowledgements.* This research is produced as part of the FWF Austrian Science Fund project S 11603-N16. In part the calculations were performed on the hpc-bw-cluster (University of Tübingen, Germany).

## References

- Agnor, C. & Asphaug, E. 2004, *ApJ*, 613, L157  
 Agnor, C. B., Canup, R. M., & Levison, H. F. 1999, *Icarus*, 142, 219  
 Alexander, S. G. & Agnor, C. B. 1998, *Icarus*, 132, 113  
 Asphaug, E. 2009, *Annual Review of Earth and Planetary Sciences*, 37, 413  
 Asphaug, E. 2010, *Chemie der Erde / Geochemistry*, 70, 199  
 Baer, J. & Chesley, S. R. 2008, *Celestial Mechanics and Dynamical Astronomy*, 100, 27  
 Benavidez, P. G., Durda, D. D., Enke, B. L., et al. 2012, *Icarus*, 219, 57  
 Benz, W. & Asphaug, E. 1994, *Icarus*, 107, 98  
 Benz, W. & Asphaug, E. 1995, *Computer Physics Communications*, 87, 253  
 Benz, W. & Asphaug, E. 1999, *Icarus*, 142, 5  
 Canup, R. M., Barr, A. C., & Crawford, D. A. 2013, *Icarus*, 222, 200  
 Dvorak, R., Eggl, S., Süli, Á., et al. 2012, in *American Institute of Physics Conference Series*, Vol. 1468, American Institute of Physics Conference Series, ed. M. Robnik & V. G. Romanovski, 137–147  
 Galiazzo, M., Souami, D., & Souchay, J. 2011, in *EPSC-DPS Joint Meeting 2011*, 495  
 Genda, H., Kokubo, E., & Ida, S. 2012, *ApJ*, 744, 137  
 Geretshauser, R. J., Speith, R., & Kley, W. 2011, *A&A*, 536, A104  
 Gingold, R. A. & Monaghan, J. J. 1977, *MNRAS*, 181, 375  
 Grady, D. E. & Kipp, M. E. 1980, *International Journal of Rock Mechanics and Mining Sciences & Geomechanics Abstracts*, 17, 147  
 Jutzi, M. & Asphaug, E. 2011, *Nature*, 476, 69  
 Jutzi, M., Benz, W., & Michel, P. 2008, *Icarus*, 198, 242  
 Jutzi, M., Michel, P., Hiraoka, K., Nakamura, A. M., & Benz, W. 2009, *Icarus*, 201, 802  
 Knežević, Z. & Milani, A. 2003, *A&A*, 403, 1165  
 Kokubo, E. & Genda, H. 2010, *ApJ*, 714, L21  
 Lange, M. A., Ahrens, T. J., & Boslough, M. B. 1984, *Icarus*, 58, 383  
 Leinhardt, Z. M. & Stewart, S. T. 2012, *ApJ*, 745, 79  
 Libersky, L. D. & Petschek, A. G. 1991, in *Lecture Notes in Physics*, Berlin Springer Verlag, Vol. 395, *Advances in the Free-Lagrange Method Including Contributions on Adaptive Gridding and the Smooth Particle Hydrodynamics Method*, ed. H. E. Trease, M. F. Fritts, & W. P. Crowley, 248–257  
 Lucy, L. B. 1977, *AJ*, 82, 1013  
 Lunine, J. I., O’Brien, D. P., Raymond, S. N., et al. 2011, *Advanced Science Letters*, 4, 325  
 Maindl, T. I. & Dvorak, R. 2013, *ArXiv e-prints*  
 Maindl, T. I., Schäfer, C., Speith, R., et al. 2013, *Astronomische Nachrichten*, 334, 996  
 Marcus, R. A., Sasselov, D., Stewart, S. T., & Hernquist, L. 2010, *ApJ*, 719, L45  
 Marcus, R. A., Stewart, S. T., Sasselov, D., & Hernquist, L. 2009, *ApJ*, 700, L118  
 Melosh, H. J. 1989, *Impact cratering: A geologic process* (Oxford University Press, New York)  
 Melosh, H. J. & Ryan, E. V. 1997, *Icarus*, 129, 562  
 Michel, P., Benz, W., & Richardson, D. C. 2004, *Planet. Space Sci.*, 52, 1109  
 Monaghan, J. J. 2005, *Reports on Progress in Physics*, 68, 1703  
 Nakamura, A. M., Michel, P., & Setoh, M. 2007, *Journal of Geophysical Research (Planets)*, 112, 2001  
 Nouda, A., Emori, H., & Nakazawa, K. 2009, *Earth, Planets, and Space*, 61, 779  
 Riecker, S. T. 2014, Master thesis, Eberhard-Karls-Universität Tübingen  
 Rosswog, S. 2009, *New A Rev.*, 53, 78  
 Schäfer, C., Speith, R., Hipp, M., & Kley, W. 2004, *A&A*, 418, 325  
 Schäfer, C., Speith, R., & Kley, W. 2007, *A&A*, 470, 733  
 Tillotson, J. H. 1962, *Metallic Equations of State for Hypervelocity Impact*, Tech. Rep. General Atomic Report GA-3216, General Dynamics, San Diego, CA  
 Weibull, W. A. 1939, *Ingvetensk. Akad. Handl.*, 151, 5